Journal of Power Sources 186 (2009) 428–434

Contents lists available at ScienceDirect

Journal of Power Sources

journal homepage: www.elsevier.com/locate/jpowsour

Oxidation resistance and electrical properties of anodically electrodeposited Mn–Co oxide coatings for solid oxide fuel cell interconnect applications

Weifeng Wei*, Weixing Chen, Douglas G. Ivey

Department of Chemical and Materials Engineering, University of Alberta, Edmonton, Alberta, Canada T6G 2G6

ARTICLE INFO

Article history:
Received 3 September 2008
Received in revised form
29 September 2008
Accepted 30 September 2008
Available online 17 October 2008

Keywords:
Solid oxide fuel cells
Ferritic stainless steel interconnects
Mn–Co spinel coatings
Anodic electrodeposition

ABSTRACT

Co-rich and crack-free Mn–Co oxide coatings were deposited on AISI 430 substrates by anodic electrodeposition from aqueous solutions. The as-deposited Mn–Co oxide coatings, with nano-scale fibrous morphology and a metastable rock salt-type structure, evolved into a $(Cr,Mn,Co)_3O_4$ spinel layer due to the outward diffusion of Cr from the AISI 430 substrates when pretreated in air. The Mn–Co oxide coatings were reduced into metallic Co and Mn_3O_4 phases when annealed in a reducing atmosphere of 5% H_2–95% N_2. In contrast to the degraded oxidation resistance and electrical properties observed for the air-pretreated Mn–Co oxide coated samples, the H_2-pretreated Mn–Co oxide coatings not only acted as a protective barrier to reduce the Cr outward diffusion, but also improved the electrical performance of the steel interconnects. The improvement in electronic conductivity can be ascribed to the higher electronic conductivity of the Co-rich spinel layer and better adhesion of the scale to the steel substrate, thereby eliminating scale spallation.

1. Introduction

The anode-supported solid oxide fuel cell (SOFC) design, with a very thin electrolyte (<20 μm thick), allows SOFC stacks to operate at intermediate temperatures ranging from 650 to 800 °C [1–5]. The reduction of the operating temperature makes it possible to use metallic interconnects to replace expensive ceramic-based interconnects such as $LaCrO_3$. Ferritic stainless steels, as a result of their good mechanical properties, thermal and electronic conductivity, ease of fabrication and very low cost, are among the most promising materials for SOFC interconnects. However, bare ferritic stainless steels tend to form a chromia scale at the operating temperatures. Rapid growth of the chromia scale leads to a high contact resistance and, in turn, deteriorates the long-term cell performance. Volatile Cr species from the chromia scale may form in the presence of water vapor, and these species can poison the cathode or the cathode–electrolyte interface [6,7]. One approach to overcome these problems is through the application of a protective coating on the stainless steel interconnect. The materials for a protective coating ought to have high electrical conductivity and low chromium cation and oxygen anion diffusivity at the operating temperatures.

Perovskite oxides, such as $(La,Sr)CrO_3$, $(La,Sr)CoO_3$ and $(La,Sr)MnO_3$, have been extensively evaluated as coating materials during the past decade [8–20]. Generally, chromites, which exhibit a lower oxygen ionic conductivity than other perovskite compositions such as cobaltites [16–18], provide better protection to the metal substrates by inhibiting scale growth beneath the perovskite layer. However, one potential concern is the fact that the chromites will release volatile Cr species, although at a relatively low rate [21,22], which may still lead to an unacceptable degradation in cell performance. In comparison, Cr-free perovskites such as cobaltites, with higher electrical conductivity and higher ionic conductivity, offer more effective reduction in contact resistance. However, the higher ionic conductivity leads to a higher growth rate of the scale beneath the protective layer, thus offsetting the high electrical conductivity. Furthermore, fast diffusion of Cr through the non-chromium perovskite layers will eventually result in the presence of Cr at the surface of the protective layer and subsequent cell poisoning.

In addition to the perovskites, spinel oxides have also been introduced as protective coatings for ferritic stainless steel interconnects in SOFCs. A Mn–Co spinel protective layer appears to be an effective barrier to both Cr outward and O inward transport, as indicated by long-term evaluations [23]. The mechanical stability of the spinel protective layer and its effectiveness as a chromium mass barrier are not affected by thermal cycling [23]. Moreover, with a higher electrical conductivity than that of chromia and Cr-containing spinels [24,25], Mn–Co spinel protective layers drastically reduce the interfacial contact resistance. Typical preparation methods for oxide coatings are thermal spraying [26], slurry spray-

* Corresponding author. Tel.: +1 780 492 8849; fax: +1 780 492 2881.
E-mail address: weifeng@ualberta.ca (W. Wei).

0378-7753/$ – see front matter © 2008 Elsevier B.V. All rights reserved.
doi:10.1016/j.jpowsour.2008.09.114

ing [23,27], screen printing [28] and sol–gel processing [29]. The first three techniques are generally not applicable to obtain conformal coatings on substrates with complex shapes, while sol–gel processing has relatively low deposition rates.

Electrochemical deposition has several distinct advantages over the techniques mentioned above for the preparation of oxide coating materials [30]. Firstly, uniform films can be deposited on substrates of complex shape with a high degree of reproducibility and film thickness can be precisely controlled by simply changing the delivered electrical charge. In addition, the low processing temperatures (often room temperature) of electrochemical deposition minimize interdiffusion. The composition and defect chemistry can be controlled through the applied overpotential and the technique setup is not capital intensive. Inspired by these considerations, anodic electrodepostion of Mn–Co oxide coatings on ferritic stainless steel substrates directly from aqueous solutions have been investigated, as described previously [31]. Co-rich and crack-free Mn–Co oxide coatings have been successfully prepared by manipulating experimental parameters, including solution composition, solution temperature and current density. The as-deposited Mn–Co oxide coatings are composed of nanocrystalline oxide particles with a defective rock salt structure [32], with a rock salt-to-spinel structural transformation occurring upon heating up to 500 °C in air [33].

The purpose of this work is to extend our previous studies on anodically deposited Mn–Co coatings to evaluate the effects of pretreating conditions, including oxidizing and reducing atmospheres, on the subsequent oxidation resistance and electrical properties of the Mn–Co oxide coatings on AISI 430 substrates.

2. Experimental procedure

2.1. Electrochemical synthesis

Mn–Co–O coatings were anodically electrodeposited on AISI 430 substrates with dimensions of 20 mm × 10 mm × 1 mm using a Gamry PC4/750 potentiostat/galvanostat. The solution consisted of 0.2 M EDTA disodium, 0.29 M $CoSO_4{\cdot}7H_2O$ and 0.01 M $MnSO_4{\cdot}H_2O$. EDTA disodium salt was added to stabilize the solutions. The three-electrode cell configuration consisted of a Pt counter electrode placed horizontally 20 mm above a horizontal AISI 430 working electrode. A saturated calomel electrode (SCE) was used as the reference electrode and all the potentials quoted are with respect to it. Before anodic deposition, the stainless steel substrates were ground with 600-grit SiC grinding paper, degreased in an alkaline solution at 80 °C and cleaned ultrasonically in deionized water. The steel substrates were anodically activated at a current density of 30 mA cm^{-2} for 2 min in 0.2 M H_2SO_4 solution and then cathodically activated at a current density of 30 mA cm^{-2} for 6 min in 0.1 M HCl solution. The deposition current density, electrolyte pH value, electrolyte temperature and deposition time were adjusted to be 5 mA cm^{-2}, 6.0, 90 °C and 90 min, respectively. During electrodeposition, agitation was introduced with a magnetically driven Teflon® coated stirring bar at a speed of 300 rpm. After electrodeposition, the working electrodes were rinsed with deionized water and dried in air.

2.2. Materials characterization

Selected Mn–Co coated samples were pretreated at 800 °C in air and forming gas (5% H_2–95% N_2) for 10 h before oxidation and electrical property analysis. Deposit microstructure, composition and morphology were analyzed in a Hitachi S-2700 scanning electron microscope (SEM), equipped with an ultra-thin window (UTW) X-ray detector, and a JAMP 9500F Auger microprobe. A JEOL 2010 transmission electron microscope (TEM), equipped with a Noran ultra-thin window (UTW) X-ray detector, was used to study the microstructure on a finer scale. Crystal structure analysis was performed using selected area electron diffraction (SAED). A Rigaku rotating Co anode XRD system, with a thin film camera attachment, was also employed for phase identification of annealed Mn–Co oxide coatings. Chemical state analysis was carried out by X-ray photoelectron spectroscopy (XPS) using a Kratos AXIS Ultra X-ray photoelectron spectrometer. A monochromatic Al source, operating at 210 W with a pass energy of 20 eV and a step of 0.1 eV, was utilized. All XPS spectra were corrected using the C 1s line at 284.6 eV. Curve fitting and background subtraction were accomplished using Casa XPS Version 2.3.13 software.

2.3. ASR measurements

The area-specific resistance (ASR) of uncoated coupons and Mn–Co oxide coated specimens, pretreated at 800 °C in air and forming gas for 10 h, were compared. The setup is similar to that described in a previous study [34]. Pre-oxidation of uncoated samples was performed at 800 °C in air for 24 h in order to prevent alloy-to-alloy adhesion. The Mn–Co–O coated specimens, with Pt wires welded on the backsides, were arranged face-to-face. No contact materials, which may affect the oxidation mechanism, were applied between the two coupons. A static load of 4.9×10^4 Pa was applied on the surface of the samples to ensure a reliable electrical contact between the samples. A constant current density of 200 mA cm^{-2} was applied and the voltage was recorded every 600 s using a PC4/750 potentiostat/galvanostat. In order to subtract the resistance contribution from the connections, Pt wires and the alloy substrates, two Pt wires were spot-welded to the sides of a single AISI 430 coupon and the resulting resistance was subtracted from the original results. All the ASR measurements mentioned above were run at 800 °C in air.

3. Results and discussion

3.1. As-deposited Mn–Co oxide coatings

The morphology and crystal structure of the as-prepared Mn–Co oxide coatings were analyzed using SEM and TEM. Plan view secondary electron (SE) images, shown in Fig. 1a, indicate that the Mn–Co oxide coatings have a rough but crack-free morphology. The high resolution SE micrograph (inset of (Fig. 1a) confirms that the oxide coatings are composed of nano-scale fibers entangled with one another. A cross-sectional backscattered electron (BSE) image of an as-deposited Mn–Co oxide coating is shown in Fig. 1b. It is apparent that the as-deposited coating is continuous and uniform with an average thickness of about 6.0 μm. The Co/Mn ratio in the as-deposited oxide coatings was determined to be 53:47 using EDX analysis. Fig. 1c shows a dark field (DF) TEM micrograph and a corresponding SAED pattern taken from an as-deposited Mn–Co–O coating. The DF TEM image reveals that the nano-scale fibers are not individual oxide crystals, but are composed of equiaxed oxide nanocrystals with a diameter less than 10 nm. The continuous SAED ring pattern also confirms their nanocrystalline nature. The d-spacings measured from the SAED pattern (inset of Fig. 1c) are consistent with face-centered cubic (FCC) MnO (JCPDS card No. 07-0230) with a space group of $Fm\bar{3}m$. The diffracted rings were indexed as (1 1 1), (2 0 0), (2 2 0), (3 1 1) and (2 2 2), respectively, as shown in the inset of Fig. 1c. The structural information is in agreement with our previous study [32].

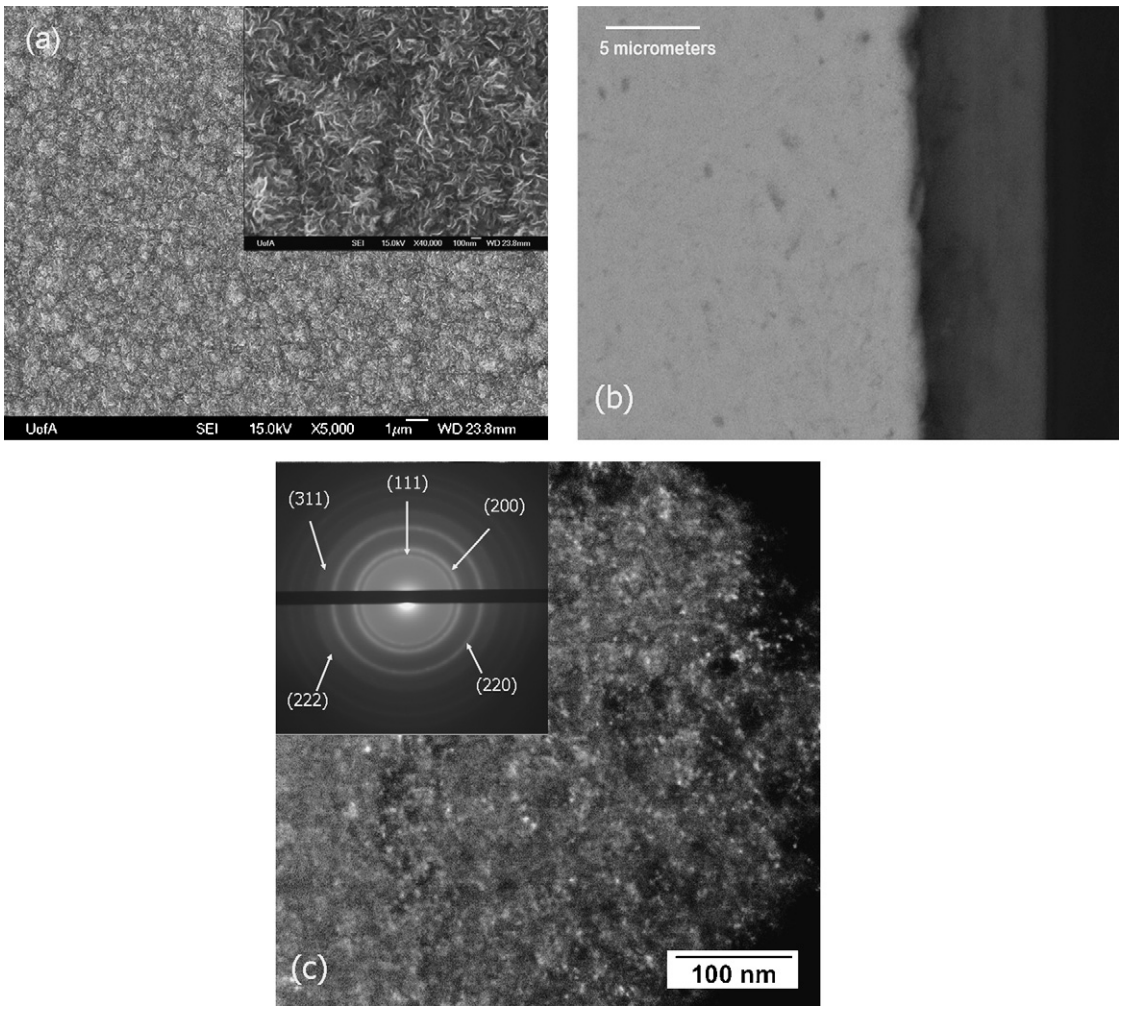

Fig. 1. Morphology and crystal structure of as-deposited Mn–Co oxide coating. (a) Plan view SE images; (b) cross-sectional BSE image; (c) DF TEM micrograph and a corresponding SAED pattern.

3.2. Air-pretreated Mn–Co oxide coatings

Fig. 2a shows a representative plan view SE image of a Mn–Co oxide coating annealed at 800 °C for 10 h in air. On the surface of the nanocrystalline oxide grains, there are several scattered micron-scale oxide crystals. A high resolution SE micrograph (inset of Fig. 2a) reveals that the initial fibrous morphology has evolved into equiaxed nanocrystals with grain sizes ranging from 100 to 300 nm. A cross-sectional BSE image of the annealed Mn–Co oxide coating is depicted in Fig. 2b. Three sublayers were detected in the ~5.0 μm oxide scale, which is slightly thinner than the as-deposited Mn–Co oxide coating. This implies that annealing induces densification of the as-deposited coating. Delamination of the oxide layer is apparent, shown as the dark inner layer in Fig. 2b. EDX line scan (Fig. 2b) confirms that the material adjacent to the delaminated region is silicon-rich. The intermediate sublayer is composed of nanocrystalline oxide grains and the outer sublayer consists of micro-scale oxide grains. Micro-cracking is also visible within the intermediate sublayer, as shown by the arrows in Fig. 2b. It is apparent from the EDX line scans that the intermediate and outer sublayers are quite homogeneous in composition. Chromium, Mn and Co are the three major elements within the two sublayers. Outward diffusion of Cr and Mn from the stainless steel substrate has made the entire oxide scale Cr–Mn–Co-rich.

The thin film XRD pattern (an incident angle of 5°) in Fig. 2c reveals that two major phases, Cr_2O_3 and $(Cr,Mn,Co)_3O_4$, exist in the oxide coating annealed in air. Based on the BSE images and EDX line scan results in Fig. 2b, the chromium is evenly distributed within the entire oxide layer. Mass transport and the interfacial reactions can be envisioned as follows. The as-deposited Mn–Co oxide coatings are porous and have a metastable rock salt-type structure. A rock salt-to-spinel structural transformation occurs in the oxide coatings when annealed at a temperature of 500 °C [33]. The structural transformation involves the migration of Mn/Co cations from the octahedral interstices to the tetrahedral interstices, which is accompanied by the reduction of Mn/Co cations and the release of oxygen [33]. As discussed in previous work [32], the average valences for Mn and Co cations in the as-deposited Mn–Co oxide coatings are estimated to be +3.5 and +2 to +3, respectively. Considering that the Mn/Co ratio is close to 1, the reduction reaction occurring in the oxide coating during annealing in air is:

$$3MnO_{1.75} + 3CoO_x\,(1 < x < 1.5) \rightarrow 2(Mn,Co)_3O_4 + \frac{(3x - 2.75)}{2}O_2 \uparrow \quad (1)$$

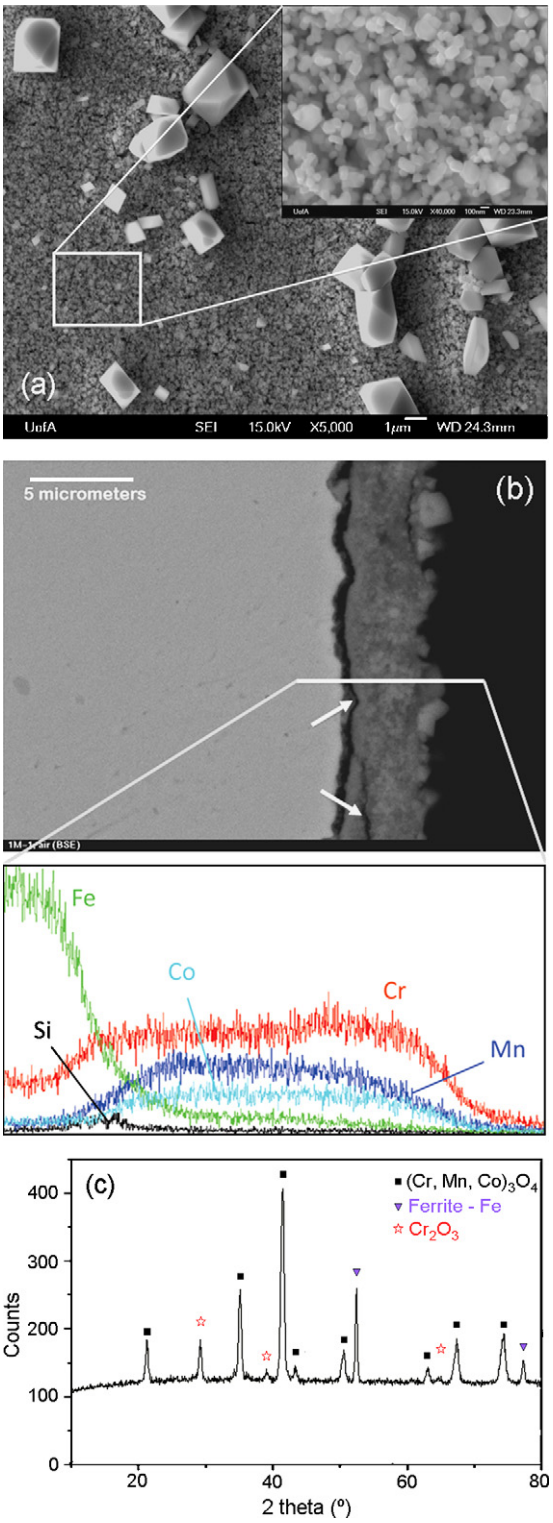

Fig. 2. Morphology, chemistry and crystal structure of the air-pretreated Mn–Co oxide coating. (a) Plan view SE images; (b) cross-sectional BSE image and EDX line scan; (c) thin film XRD pattern.

The released oxygen generates a high oxygen partial pressure within the oxide coating, which facilitates the outward diffusion of Cr to form the Cr–Mn–Co-rich spinel phase in the oxide coating. In this case, therefore, the Mn–Co oxide coatings are not protective against Cr outward diffusion.

3.3. Mn–Co oxide coatings pretreated in forming gas

Fig. 3a shows a plan view SE image of a Mn–Co oxide coating annealed at 800 °C for 10 h in an atmosphere of 5% H_2–95% N_2. The coating morphology can be described as micron-scale white particles embedded in a grey matrix. A high resolution SE micrograph (inset of Fig. 3a) reveals that some voids are also present in the oxide coating, in addition to the white particles and the grey matrix. A cross-sectional BSE image of an annealed Mn–Co oxide coating is depicted in Fig. 3b. From the EDX line scan (Fig. 3b), the white particles and grey matrix are confirmed to be Co- and Mn-rich, respectively. Between the stainless steel substrate and a thin, dense chromia scale, there is discontinuous Si-rich phase; a result which is supported by the EDX line scans. It is apparent that the oxide coatings annealed in a reducing atmosphere exhibit better adhesive properties when compared with oxide coatings annealed in air.

In order to determine the chemical states of Co and Mn in the oxide coatings pretreated in forming gas, XPS was used to obtain Co 2p and Mn 3s spectra, as indicated in Fig. 3c. From the Co 2p spectrum, the binding energy of Co 2p3/2 was determined to be 778.20 eV, which is consistent with that for metallic Co [35]. The oxidation states for Mn in the oxide nanocrystals were determined by analyzing the Mn 3s XPS spectrum. The oxidation states for Mn are closely related to the 3s peak splitting widths. Based on an approximately linear relationship between the splitting width (ΔE) and the Mn oxidation state [36,37], the experimental splitting width (ΔE) in the Mn 3s spectrum (Fig. 3c) was converted into an average oxidation valence of +2.5. Therefore, the Co-rich white particles are metallic cobalt, while the Mn-rich grey matrix is Mn_3O_4. The XRD pattern in Fig. 3d also confirms the coexistence of Co, Mn_3O_4, Cr_2O_3 and SiO_2 phases for oxide coatings annealed in the reducing atmosphere. The reduction reactions occurring in the oxide coating during annealing in the forming gas are summarized as follows:

$$3MnO_{1.75} + \tfrac{5}{4}H_2 \rightarrow Mn_3O_4 + \tfrac{5}{4}H_2O \quad (2)$$

$$CoO_x\,(1 < x < 1.5) + xH_2 \rightarrow Co + xH_2O \quad (3)$$

With increasing holding time at 800 °C, newly formed Co nanoparticles will aggregate and be sintered into micron-size Co particles (Fig. 3a). The widely distributed micro-voids, observed in Fig. 3a, are probably induced by the water vapor release, as shown in the above chemical reactions.

3.4. Oxidation resistance of Mn–Co oxide coated AISI 430 substrates

The oxidation resistance and electrical properties for the Mn–Co oxide coatings, pretreated in both air and reducing atmospheres, were evaluated in air at 800 °C. Fig. 4a depicts a cross-sectional BSE image of an air-pretreated Mn–Co oxide coating after 500 h in air at 800 °C. Three sublayers are present in the oxide coating. From the EDX line scans, it is noted that besides the Cr-rich inner sublayer, the two outer sublayers are homogeneous in chemistry. The XRD pattern in Fig. 4b also confirms the existence of chromia and spinel phases in the oxide coatings. Therefore, the two outer sublayers have the same cubic spinel structure. Compared with the air-pretreated Mn–Co oxide coating (Fig. 2b), two major differences are noted. An ~2 μm thick chromia scale, covered by a spinel layer, is detectable. Underneath the scale are isolated, dark islands of silica. The adhesiveness of the oxide scale is increasingly deteriorated; parts of the oxide scale are observed to detach from the stainless steel substrate, as shown by the arrows in Fig. 4a.

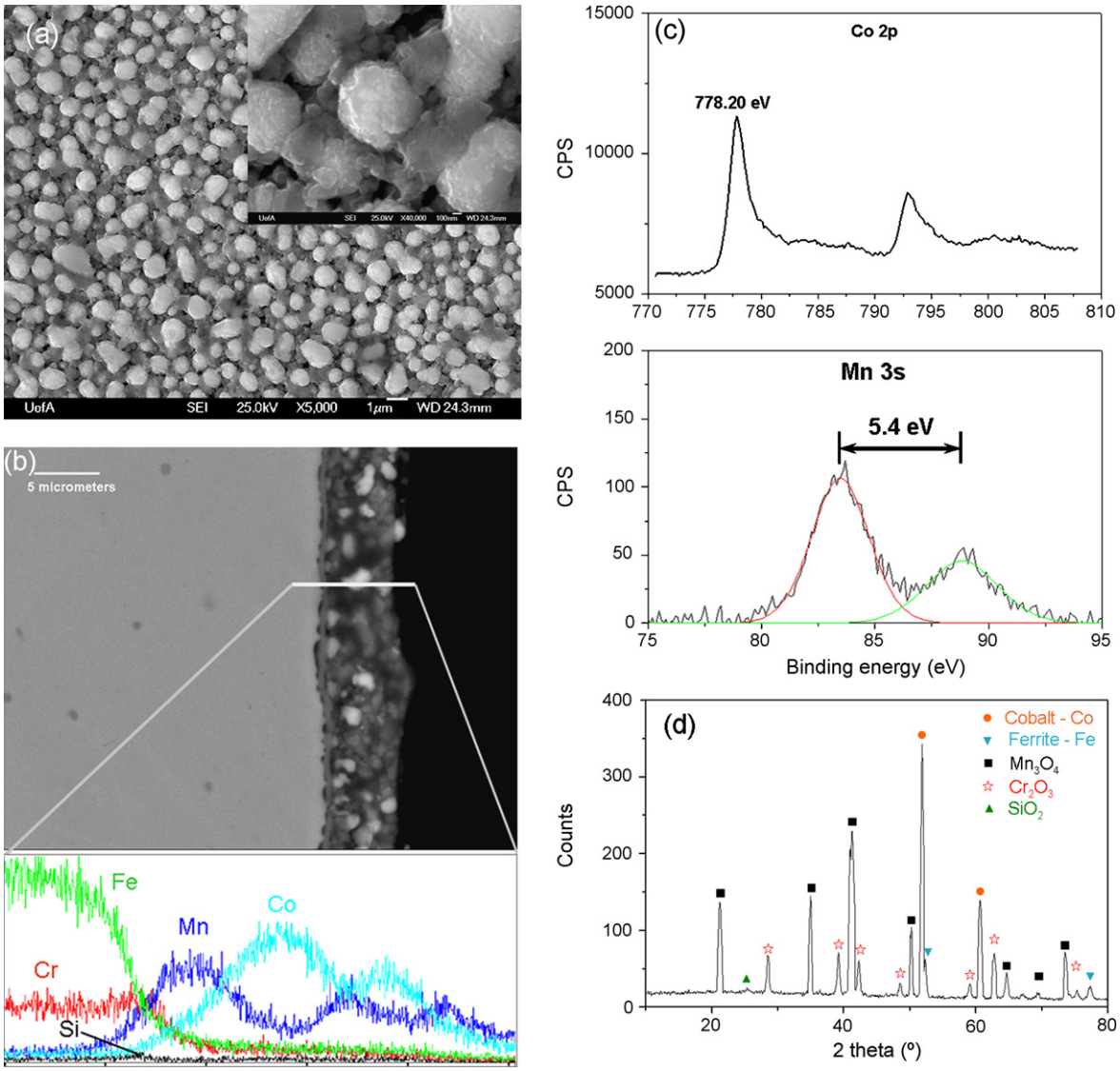

Fig. 3. Morphology, chemistry and crystal structure of the forming gas pretreated Mn–Co oxide coating. (a) Plan view SE images; (b) cross-sectional BSE image and EDX line scan; (c) Mn 3s and Co 2p XPS spectra; (d) thin film XRD pattern.

The BSE image in Fig. 5a shows a cross-sectional view of a Mn–Co oxide coating, pretreated in forming gas, after 500 h at 800 °C in air. Compared with the air-pretreated sample, the spinel protective layer appears to have improved adhesion to the stainless steel substrate and is free of cracking or spallation. From the EDX line scans, a smooth, continuous interface was observed between the spinel layer and the chromia scale. The thickness of chromia scale is 2.0–2.2 μm after 500 h oxidation in air, similar to that for the air-pretreated sample. Chromium from the stainless steel substrate was also observed to diffuse into the Mn–Co oxide layer, but the Cr content is much lower than that in the air-pretreated sample and no Cr was detected on the coating surface. The XRD pattern reveals the presence of silica, chromia and $(Co,Mn,Cr)_3O_4$ cubic spinel phases in the oxide layer. The forming gas-pretreated Mn–Co oxide coating can reduce Cr outward diffusion when compared with the air-pretreated oxide coating. However, Cr from the steel substrates can still diffuse into the Mn–Co spinel layer during long-term oxidation. In order to further suppress the Cr outward diffusion, further investigation needs to be conducted to optimize the pretreating process for the Mn–Co oxide coatings.

3.5. Electrical properties for uncoated and Mn–Co oxide coated AISI 430

ASR curves for uncoated and Mn–Co–O coated AISI 430 samples, pretreated in different atmospheres, as a function of time at 800 °C in air are compared in Fig. 6. The ASR values for bare AISI 430 substrates increase rapidly to 0.026 Ω cm^2 after the first 10 h and approach 0.036 Ω cm^2 after 300 h, with a parabolic growth tendency. For the air-pretreated Mn–Co oxide coated samples, similar ASR values were observed for the first 200 h compared with those for bare AISI 430 steel. After 200 h, the ASR values exhibit a more significant increase reaching 0.060 Ω cm^2 after 500 h of oxidation. The air-pretreated Mn–Co oxide coated samples exhibit degraded electrical performance compared with bare AISI 430, which can probably be attributed to the rapid growth of oxide scale due to Cr outward diffusion and the poor adhesion between the oxide scale and the steel substrate (Fig. 4a).

In contrast, the ASR values for forming gas pretreated Mn–Co oxide coatings show a different trend. A very low electrical resistance (ASR < 0.01 Ω cm^2) was detected for up to 100 h oxidation in air, followed by a parabolic increase in ASR to level off at a con-

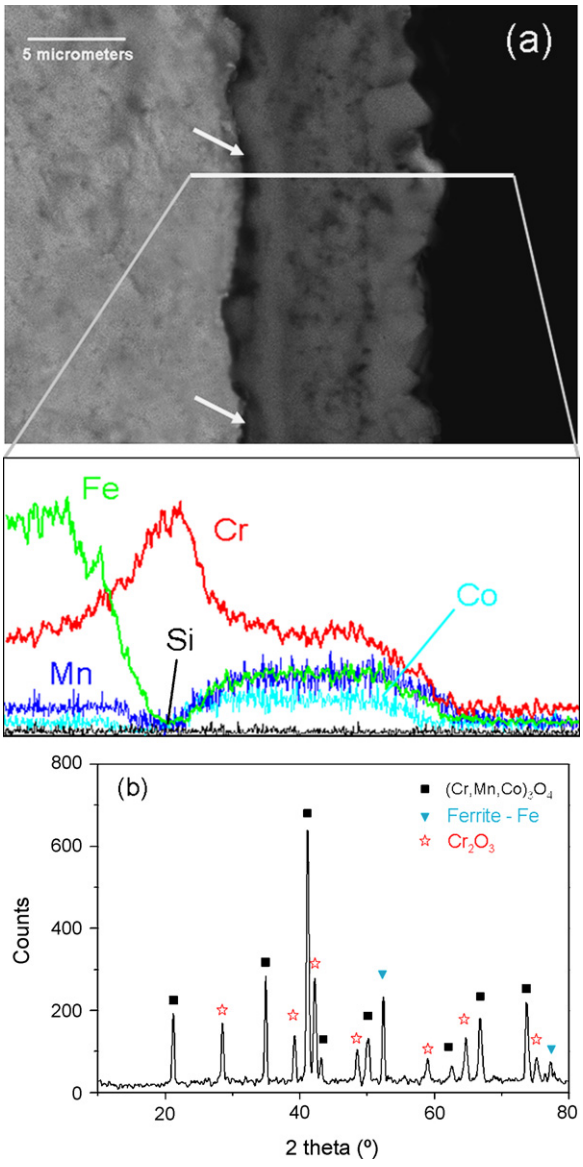

Fig. 4. Morphology, chemistry and crystal structure of the air-pretreated Mn–Co oxide coating after 500 h in air at 800 °C. (a) Cross-sectional BSE image and EDX line scan and (b) thin film XRD patterns.

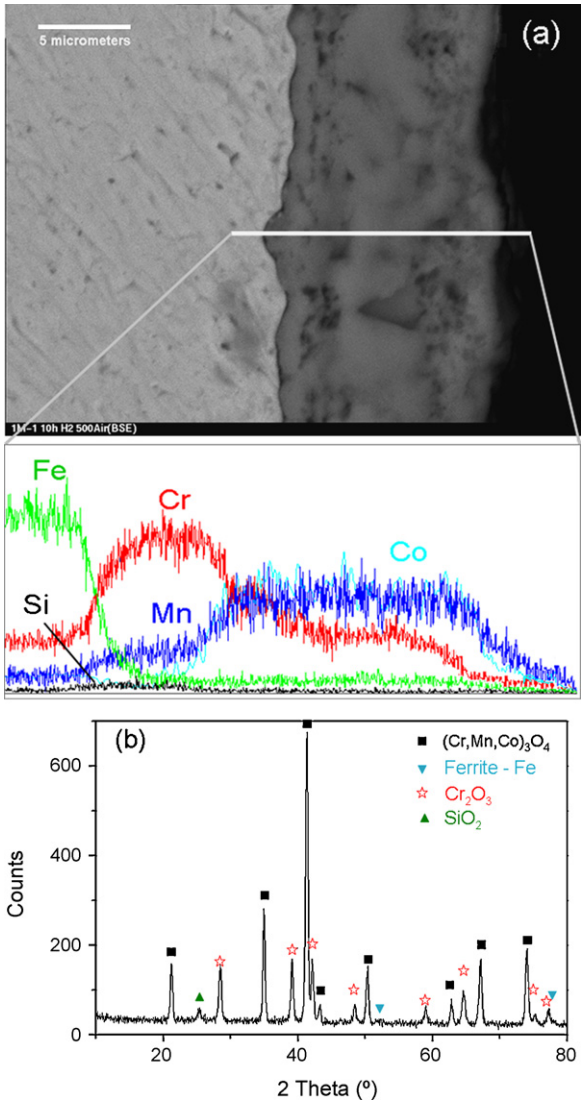

Fig. 5. Morphology, chemistry and crystal structure of the forming gas pretreated Mn–Co oxide coating after 500 h in air at 800 °C. (a) Cross-sectional BSE image and EDX line scan and (b) thin film XRD pattern.

stant value of 0.025 Ω cm^2 after 500 h of oxidation. The starting ASR value for the air-pretreated Mn–Co oxide coated samples is about 0.020 Ω cm^2 higher than that for the forming gas pretreated Mn–Co oxide coated samples. The difference in ASR values is further raised to 0.035 Ω cm^2 after 500 h oxidation. Based on Figs. 4a and 5a, the thickness values of the chromia scale and spinel protective layer in these two oxide coatings are comparable, so that the improved electronic conductivity for the forming gas pretreated Mn–Co oxide coatings can be ascribed to the higher electronic conductivity of the spinel layer with a high Co content and improved adhesion of the scale to the steel substrate.

4. Summary

Crack-free Mn–Co oxide coatings, with a Co/Mn ratio of 53:47, were deposited onto AISI 430 substrates by anodic electrodeposition from aqueous solutions. The as-deposited Mn–Co oxide coatings are composed of nano-scale fibers entangled with each other and have a defective rock salt-type structure. The Mn–Co

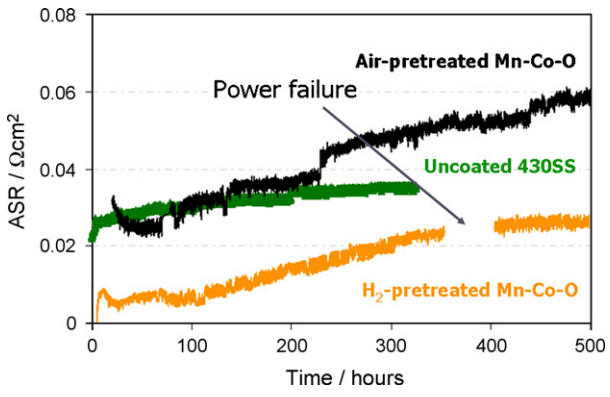

Fig. 6. ASR analysis of uncoated and Mn–Co oxide coated AISI 430 samples.

oxide coatings evolve into a $(Cr,Mn,Co)_3O_4$ spinel layer due to the outward diffusion of Cr from the AISI 430 substrates, when pretreated at 800 °C in air for 10 h. The Mn–Co oxide coatings are reduced into metallic Co and Mn_3O_4 phases when annealed in a reducing atmosphere of 5% H_2–95% N_2 at 800 °C for 10 h. In contrast to the degraded oxidation resistance and electrical properties observed for the air-pretreated Mn–Co oxide coated samples, the forming gas pretreated Mn–Co oxide coatings not only acted as a protective barrier to reduce the Cr outward diffusion, but also improved the electrical performance of the AISI 430 substrates. The improvement in electronic conductivity can be ascribed to the high electronic conductivity of the spinel layer with a higher Co content and better adhesion of the scale to the steel substrate.

Acknowledgments

The authors are grateful to the Natural Sciences and Engineering Research Council (NSERC) of Canada and Versa Power Systems (VPS) for providing funding for this project. The Alberta Centre for Surface Engineering and Science (ACSES) is also acknowledged for providing the XPS analysis.

References

[1] H. Kabs, U. Stimming, D. Stovers, Proceedings of the Fifth International Symposium on Solid Oxide Fuel Cells, Aachen, Germany, June 1997, The Electrochemical Society, Pennington, NJ, 1997, pp. 160–170.
[2] K. Foger, R. Donelson, R. Ratnaraj, Proceedings of the Sixth International Symposium on Solid Oxide Fuel Cells, Honolulu, Hawaii, October 1999, The Electrochemical Society, Pennington, NJ, 1999, pp. 95–100.
[3] L.G.J. DeHaart, I.C. Vinke, A. Janke, H. Ringel, F. Tietz, Proceedings of the Seventh International Symposium on Solid Oxide Fuel Cells, Tsukuba, Ibaraki, Japan, June 2001, The Electrochemical Society, Pennington, NJ, 2001, pp. 111–119.
[4] I. Yasuda, Y. Baba, T. Ogiwara, H. Yakabe, Y. Matsuzaki, Proceedings of the Seventh International Symposium on Solid Oxide Fuel Cells, Tsukuba, Ibaraki, Japan, June 2001, The Electrochemical Society, Pennington, NJ, 2001, pp. 131–139.
[5] J.W. Kim, A.V. Virkar, K.Z. Fung, K. Mehta, S.C. Singhal, J. Electrochem. Soc. 146 (1999) 69–78.
[6] S.P.S. Badwal, R. Deller, K. Foger, Y. Ramprakash, J.P. Zhang, Solid State Ionics 99 (1997) 297–310.
[7] Y. Matsuzaki, I. Yasuda, Solid State Ionics 132 (2000) 271–278.
[8] S. Linderoth, Surf. Coat. Technol. 80 (1996) 185.
[9] N. Sakai, K. Yamaji, T. Horita, M. Lshikawa, H. Yokokawa, M. Dokiya, Proceedings of the 3rd European SOFC Forum, Lucerne, European Fuel Cell Forum, 1998, pp. 333–342.
[10] T. Kadowaki, T. Shiomitsu, E. Matsuda, H. Nakagawa, H. Tsuneisumi, Solid State Ionics 67 (1993) 65–69.
[11] E. Batawi, K. Honegger, D. Diethelm, M. Wettstein, Proceedings of the 2nd European SOFC Forum, Lucerne, European Fuel Cell Forum, 1996, pp. 307–314.
[12] K. Fujita, K. Ogasawara, Y. Matsuzaki, T. Sakurai, J. Power Sources 131 (2004) 261–269.
[13] S. Elangovan, S. Balagopal, M. Timper, I. Bay, D. Larsen, J. Hartvigsen, J. Mater. Eng. Perform. 13 (2004) 265–273.
[14] C. Johnson, R. Gemmen, N. Orlovskaya, Composite B 35 (2004) 167–172.
[15] N. Orlovskaya, A. Coratolo, C. Johnson, R. Gemmen, J. Am. Ceram. Soc. 87 (2004) 1981–1987.
[16] H.U. Anderson, Solid State Ionics 52 (1992) 33–41.
[17] J.W. Stevenson, T.R. Armstrong, R.D. Carneim, L.R. Pederson, W.J. Weber, J. Electrochem. Soc. 143 (1996) 2722–2729.
[18] H. Ullmann, N. Trofimenko, Solid State Ionics 119 (1999) 1–8.
[19] H. Ullmann, N. Trofimenko, F. Tietz, D. Stover, A. Ahmad-Khanlou, Solid State Ionics 138 (2000) 79–90.
[20] Z. Yang, G.G. Xia, G.D. Maupin, J.W. Stevenson, J. Electrochem. Soc. 153 (2006) 1852–1858.
[21] K. Hilpert, D. Das, M. Miller, D.P. Peck, R. Wei, J. Electrochem. Soc. 143 (1996) 3642–3647.
[22] C.C. Gindorf, L. Singheiser, K. Hilpert, Steel Res. 72 (2001) 528–533.
[23] Z. Yang, G.G. Xia, S.P. Simner, J.W. Stevenson, J. Electrochem. Soc. 152 (2005) 1896–1901.
[24] T. Yokoyama, Y. Abe, T. Meguro, K. Komeya, K. Kondo, S. Kaneko, T. Sasamoto, Jpn. J. Appl. Phys. 35 (1996) 5775–5780.
[25] Z. Yang, X.H. Li, G.D. Maupin, P. Singh, S.P. Simner, J.W. Stevenson, G.G. Xia, X.D. Zhao, Ceram. Sci. Eng. Proc. 27 (2006) 231–240.
[26] P. Fauchais, R. Etchart-Salas, V. Rat, J.F. Coudert, N. Caron, K. Wittmann-Teneze, J. Therm. Spray Technol. 17 (2008) 31–59.
[27] X. Chen, P.Y. Hou, C.P. Jacobson, S.J. Visco, L.C. De Jonghe, Solid State Ionics 176 (2005) 425–433.
[28] Z.G. Yang, G.G. Xia, S.P. Simner, J.W. Stevenson, Electrochem. Solid-State Lett. 8 (2005) A168–A170.
[29] B. Hua, J. Pu, J. Wei Gong, f. Zhang, F.S. Lu, L. Jian, J. Power Sources 185 (2008) 419–422.
[30] G. Hodes, Electrochemistry of Nanomaterials, Wiley–VCH, Weinheim, 2001, p. 67–101.
[31] W.F. Wei, W.X. Chen, D.G. Ivey, Chem. Mater. 19 (2007) 2816–2822.
[32] W.F. Wei, W.X. Chen, D.G. Ivey, J. Phys. Chem. C 111 (2007) 10398–10403.
[33] W.F. Wei, W.X. Chen, D.G. Ivey, Chem. Mater. 20 (2008) 1941–1947.
[34] N. Shaigan, D.G. Ivey, W. Chen, J. Power Sources 183 (2008) 651–659.
[35] J. Haber, L. Ungier, J. Electron Spectrosc. Relat. Phenom. 12 (1977) 305.
[36] B. Djurfors, J.N. Broughton, M.J. Brett, D.G. Ivey, Acta Mater. 53 (2005) 957–965.
[37] M. Nakayama, A. Tanaka, Y. Sato, T. Tonosaki, K. Ogura, Langmuir 21 (2005) 5907–5913.